Journal of Environmental Economics & Chemical Processes (JEECP)

https://doi.org/10.22034/jeecp.2026.735014

Journal homepage: *WWW.JEECPJournal.com*

Journal of Environmental Economics & Chemical Processes (JEECP)

ORIGINAL RESEARCH PAPER

Evaluating the Ion Adsorption Properties of CB_3 and CN_3 Nanoflakes for Nitrate and Nitrite Removal in Water Purification: A DFT Approach

Mahdi Rezaei-Sameti*, Ashkan Bagheri, Mahnaz Abasi

Department of Applied Chemistry, Faculty of Science, Malayer University, Malayer, 65174, Iran.

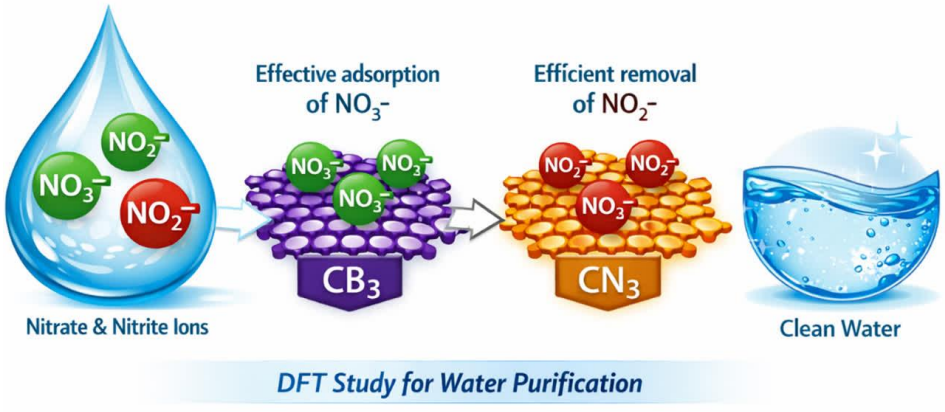
P A P E R I N F O

Paper history:
Received 06/13/2024
Accepted in revised form 08/25/2024

Keywords:
NO_3^-, NO_2^- ions
CB_3 and CN_3 nanoflakes
DFT
AIM

A B S T R A C T

In this study, the adsorption and sensing performance of nitrate (NO_3^-) and nitrite (NO_2^-) ions on CB_3 and CN_3 nanoflakes were systematically investigated in both gas and aqueous environments. Density functional theory (DFT) and time-dependent DFT (TD-DFT) calculations were performed at the ωB97XD/6-31+G (d, p) level to optimize the geometries and evaluate the electronic, thermodynamic, and sensing-related properties of the NO_3^-/NO_2^-@CB_3 and NO_3^-/NO_2^-@CN_3 complexes. The calculated adsorption energies reveal that the CB_3–NO_2^- (model 2) complex exhibits the strongest interaction among all studied systems, indicating that CB_3 nanoflakes are highly effective adsorbents for nitrate and nitrite ions. The dipole moments and polarizabilities of the NO_3^-@CB_3 and NO_3^-@CN_3 complexes are significantly higher than those of their NO_2^- counterparts, suggesting greater sensitivity toward nitrate ions. Thermodynamic analyses confirm that the adsorption processes are exothermic and thermodynamically spontaneous, with enthalpy changes (ΔH) showing a slight decrease as the temperature increases from 298.15 to 328.15 K. The reduced energy gap (E_{gap}) and chemical hardness (η) values for the adsorbed complexes indicate enhanced electrical conductivity and reactivity, supporting their suitability as sensitive sensors and efficient adsorbents. Further insights from atoms-in-molecules (AIM), electron localization function (ELF), and reduced density gradient (RDG) analyses demonstrate that the dominant interactions between NO_3^-/NO_2^- ions and CB_3/CN_3 nanoflakes are governed by electrostatic forces and van der Waals interactions, with the NO_3^-@CN_3 complex exhibiting the strongest interaction characteristics. Overall, the findings highlight CB_3 and CN_3 nanoflakes as promising candidates for the development of high-performance sensors and adsorbents for nitrate and nitrite ion removal from environmental systems.



1. Introduction

Nitrate (NO_3^-) and nitrite (NO_2^-) contamination of water resources represents a critical environmental and public health challenge worldwide, largely arising from intensive agricultural activities, excessive use of nitrogen-based fertilizers, livestock waste, industrial effluents, and improper wastewater management. Once introduced into aquatic systems, these nitrogenous species exhibit high mobility and persistence, enabling their accumulation in surface and groundwater. Acute exposure to elevated nitrate and nitrite levels is well known to cause infant methemoglobinemia, commonly referred to as "blue baby syndrome," due to the oxidation of hemoglobin and impaired oxygen transport. Moreover, long-term and chronic exposure has been associated with increased risks of carcinogenesis, endocrine disruption, and reproductive disorders, primarily through endogenous nitrosation pathways leading to the formation of N-nitroso compounds [1–4]. From an environmental perspective, excessive nitrate loading accelerates eutrophication processes, resulting in algal blooms, hypoxia, and severe degradation of aquatic ecosystems. The convergence of hydrological, toxicological, and epidemiological evidence highlights the urgent need for efficient, sustainable, and selective strategies for nitrate and nitrite removal and detection in water systems.

In recent years, nanomaterials have emerged as promising platforms for environmental remediation and chemical sensing owing to their unique

* Corresponding author: Mahdi Rezaei-Sameti
E-mail address: mrsameti@malayeru.ac.ir
ISSN: 3116-0050
URL: https://www.jeecpjournal.com/article_735014.html
Please cite this article as: M. Rezaei-Sameti, A. Bagheri, M. Abasi. *Journal of Environmental Economics & Chemical Processes (JEECP)*, 2025, **2(2)**, 65-73.
/© 2025 The Author(s). Published by Institute of Power, Movement, and Innovative Insight

physicochemical properties. Among them, graphene, a two-dimensional single-layer carbon nanoflake, has attracted considerable attention due to its exceptional mechanical strength, high electrical conductivity, large specific surface area, and remarkable chemical stability. Graphene can be synthesized through several methods, including mechanical exfoliation, chemical vapor deposition, and chemical reduction techniques [5–8]. Each carbon atom in graphene is covalently bonded to three neighboring carbon atoms via sp^2 hybridization, resulting in a robust honeycomb lattice. The atomically flat structure of graphene enables strong interactions with adsorbates on both sides of the sheet, making it an attractive candidate for adsorption and sensing applications.

To overcome limitations associated with pristine graphene, such as its zero band gap and limited selectivity, extensive efforts have been devoted to modifying its electronic and chemical properties. In this context, graphene-like nanostructures composed of boron and nitrogen atoms have gained significant interest. These heteroatom-doped or heterostructure materials exhibit tunable band gaps, enhanced chemical reactivity, and improved sensitivity toward various analytes [9–12]. Owing to their wide band gap, high structural and chemical stability, excellent mechanical strength, strong oxidation resistance, favorable thermal and electrical conductivity, and low toxicity, graphene-like boron- and nitrogen-containing nanomaterials have also attracted attention in pharmaceutical, biological, and environmental applications [13–17].
Nanoadsorbents, in particular, have demonstrated great potential for the removal of toxic metal ions as well as organic and inorganic pollutants from water and wastewater systems. Their performance advantages stem from nanoscale dimensions, exceptionally high surface-to-volume ratios, abundant active adsorption sites, high reactivity, catalytic capabilities, and ease of separation and regeneration [18]. These attributes have enabled their use in adsorption, separation, and preconcentration processes for a wide range of environmental contaminants. Continued exploration of novel nanoadsorbent materials is therefore essential to fully exploit their capabilities in sustainable environmental remediation technologies. Several theoretical and computational studies have highlighted the effectiveness of carbon-based and heteroatom-doped nanostructures for nitrogen-containing pollutant adsorption and sensing. Beheshtian et al. investigated nitrate ion adsorption on single-walled carbon nanotubes in both gas and aqueous phases, reporting energetically favorable adsorption in the gas phase with a large adsorption energy of −1.30 eV, while the process became endothermic in solvent environments [19]. In a related study, Beheshtian et al. demonstrated that the electronic band gap of the $B_{12}N_{12}$ nanocluster is highly sensitive to NO_2 adsorption, decreasing dramatically from 6.84 eV in the pristine cluster to 3.23 eV in the most stable NO_2–cluster complex. This pronounced band gap reduction significantly enhances electrical conductivity, indicating strong potential for NO_2 gas sensing applications [20]. Babar et al. [21] examined the adsorption behavior of common gaseous pollutants (CO, NO, NO_2, and NH_3) on monolayer C_3N using first-principles calculations. Their results revealed that all molecules are physisorbed, with NO and NO_2 exhibiting particularly high sensing sensitivity and excellent recovery times, especially for NO detection. Similarly, Yuan et al. [22] demonstrated that $B_3C_2P_3$ monolayers exhibit outstanding sensitivity and selectivity toward NO_2 and NO gases under ambient conditions, maintaining reliable sensing performance even in the presence of moisture, O_2, and CO_2. Villanueva-Mejia et al. [23] explored the electronic and magnetic responses of carbon-doped boron nitride nanoribbons upon adsorption of nitro species, revealing adsorption-induced magnetic transitions and, in some cases, molecular dissociation. Ashishie et al. [24] further reported that graphene doped with boron and nitrogen heteroatoms shows enhanced adsorption capability and electrical conductivity for CO_2 and NO_2 gases, attributed to a significant reduction in the energy gap. Additionally, Hu et al. [25] identified the $B_3C_2P_3$ monolayer as an excellent sensing material for NH_3, NO_2, and NO, exhibiting strong chemical adsorption for NH_3 and NO_2 and favorable physical adsorption for NO. Despite these advances, most previous studies have focused primarily on gaseous nitrogen oxides, while the adsorption and sensing behavior of nitrate and nitrite ions, particularly in aqueous environments remain comparatively underexplored. Motivated by our previous investigations into adsorption and interaction phenomena in nanostructured materials [26–31], the present work aims to systematically examine the adsorption and detection of nitrate and nitrite ions on CB_3 and CN_3 nanoflakes in both gas and water media using advanced density functional theory approaches. The outcomes of this study are expected to provide valuable insights into the design of efficient nanoadsorbents and highly sensitive sensors for monitoring and removing nitrate and nitrite ions from environmental water systems.

2. Computational Details

In this study, density functional theory (DFT) calculations were employed to evaluate the potential of CB_3 and CN_3 nanoflakes as efficient adsorbents and sensitive sensors for nitrate (NO_3^-) and nitrite (NO_2^-) ions in water and wastewater environments. Initially, the interactions of NO_3^- and NO_2^- ions with the nanoflake surfaces were examined by considering adsorption through different N–O sites (I, II, and III), as illustrated in Scheme 1. Subsequently, the most representative configurations of all $NO_3^-/NO_2^-@CB_3$ and $NO_3^-/NO_2^-@CN_3$ complexes were fully optimized using the ωB97XD exchange–correlation functional in conjunction with the 6-31+G(d,p) basis set within the DFT framework [32]. The ωB97XD functional is a long-range corrected hybrid functional based on the Becke 97 formulation, incorporating empirical dispersion corrections and employing 22% short-range Hartree–Fock exchange and 100% long-range Hartree–Fock exchange, making it particularly suitable for accurately describing noncovalent interactions. All initial molecular structures were constructed using the GaussView 06 software package [33], and all quantum chemical calculations were performed with the Gaussian 09 program [34]. Geometry optimizations were carried out using strict convergence criteria, with maximum force and displacement thresholds set to 0.00042 Hartree and 0.0018 Hartree/Bohr, respectively. Frequency calculations were subsequently performed for all optimized structures, confirming the absence of imaginary frequencies and thus verifying that all configurations correspond to true minima on the potential energy surface. Based on the optimized geometries, adsorption energies of the $NO_3^-/NO_2^-@CB_3$ and $NO_3^-/NO_2^-@CN_3$ complexes were calculated at different temperatures using Eq. (1). To ensure the accuracy of the interaction energies, basis set superposition error (BSSE) corrections were applied using the counterpoise method. The resulting adsorption energies are summarized in Table 1.

$$E_{ads} = E_{Ions\&nanoflake} - (E_{Ions} + E_{nanoflake}) + BSSE \quad (1)$$

Here, $E_{ions@nanoflake}$represents the total electronic energy of the $NO_3^-/NO_2^-@CB_3$ and $NO_3^-/NO_2^-@CN_3$ complexes, while E_{ions} and $E_{nanoflake}$denote the total electronic energies of the isolated NO_3^-/NO_2^- ions and the pristine CB_3 and CN_3 nanoflakes, respectively. The thermodynamic parameters of the $NO_3^-/NO_2^-@CB_3$ and $NO_3^-/NO_2^-@CN_3$ complexes, including enthalpy (ΔH), Gibbs free energy (ΔG), and entropy (ΔS) changes, were evaluated at temperatures of 298.15, 308.15, 318.15, and 328.15 K using Eq. (2). The calculated thermodynamic values are summarized in Table 1 and S1.

$$\Delta M = M_{Ions\&nanoflake} - (M_{Ions} + M_{nanoflake}) \qquad M: H, G \quad (2)$$

In this context, $M_{ions@nanoflakes}$, M_{ions}, and $M_{nanoflakes}$ represent the sums of the electronic and thermal enthalpies or the sums of the electronic and thermal Gibbs free energies of the $NO_3^-/NO_2^-@CB_3$ and $NO_3^-/NO_2^-@CN_3$ complexes, the isolated NO_3^-/NO_2^- ions, and the pristine CB_3 and CN_3 nanoflakes, respectively. To evaluate the influence of the solvent environment on the adsorption behavior of NO_3^- and NO_2^- ions on CB_3 and CN_3 nanoflakes, the polarizable continuum model (PCM) was employed to simulate aqueous conditions [35]. The solvation effect was quantified by calculating the change in Gibbs free energy of adsorption in solution, $\Delta\Delta G_{sol}$, using Eq. (3). The corresponding values are summarized in Table 1.

$$\Delta\Delta G_{(sol)} = \Delta G^{sol}_{Ions\&nanoflake} - \Delta G^{sol}_{Ions} - \Delta G^{sol}_{nanoflake} \quad (3)$$

$$\Delta G_{gas-sol} = \Delta G_{gas} + \Delta\Delta G_{(sol)} \quad (4)$$

Here, the solvation Gibbs free energies correspond to the $NO_3^-/NO_2^-@CB_3$ and $NO_3^-/NO_2^-@CN_3$ complexes, the isolated NO_3^-/NO_2^- ions, and the pristine CB_3 and CN_3 nanoflakes. The term $\Delta G_{gas-sol}$ denotes the Gibbs free energy change associated with transferring the $NO_3^-/NO_2^-@CB_3$ and $NO_3^-/NO_2^-@CN_3$ complexes from the gas phase to the aqueous environment. To gain deeper insight into the electronic structure, reactivity, and interaction mechanisms of the studied systems, a series of quantum chemical descriptors was evaluated. These include the energies of the highest occupied molecular orbital (E_{HOMO}) and the lowest unoccupied molecular orbital (E_{LUMO}) [36–37], which were used to assess electronic stability and charge-transfer behavior. In addition, the electron localization function (ELF) [38], infrared (IR) vibrational spectra [39], atoms-in-molecules (AIM) topological analysis [40], and reduced density gradient (RDG) analysis [41] were calculated for all $NO_3^-/NO_2^-@CB_3$ and $NO_3^-/NO_2^-@CN_3$ complexes. These analyses collectively provide a comprehensive description of the nature, strength, and spatial distribution of intermolecular interactions, and the resulting data were systematically analyzed and discussed.

3. Results and Discussion

3.1. Structural and Geometrical Parameters and Adsorption Properties

In this study, the adsorption and sensing capabilities of CB_3 and CN_3 nanoflakes toward nitrate (NO_3^-) and nitrite (NO_2^-) ions were systematically investigated at different temperatures using density functional theory (DFT) and time-dependent DFT (TD-DFT) methods. All possible $NO_3^-/NO_2^-@CB_3$ and $NO_3^-/NO_2^-@CN_3$ complexes were fully optimized at the ωB97XD/6-31+G (d,p) level of theory. Frequency calculations confirmed the absence of

imaginary frequencies for the selected stable configurations, verifying that all optimized structures correspond to true minima on the potential energy surface. The optimized geometries are illustrated in Figures 1 and S1. Structural analysis reveals that the average C–C and B–C bond lengths in the BC_3 nanoflake are 1.562 and 1.417 Å, respectively, while the corresponding C–C and N–C bond lengths in the NC_3 nanoflake are 1.428 and 1.408 Å, respectively. These values are in excellent agreement with previously reported theoretical data [42–43], confirming the reliability of the applied computational methodology.

The optimized adsorption geometries indicate strong interactions between the ions and nanoflakes. For the NO_2^-@CB_3 complexes, the shortest ion–surface distances (d_{dis}) in models 1, 2, and 3 are 1.524, 1.680, and 1.523 Å, respectively, whereas the corresponding distances for NO_2^-@CN_3 are 1.625, 2.060, and 1.560 Å. In the case of nitrate adsorption, the d_{dis} values for NO_3^-@CB_3-1, -2, and -3 are 1.656, 1.605, and 1.587 Å, respectively, while for NO_3^-@CN_3-1, -2, and -3 they are 2.280, 2.180, and 1.281 Å. These relatively short distances suggest strong ion–surface interactions, particularly for the CB_3-based complexes. Based on the optimized geometries, the adsorption energies (E_{ads}) of all NO_3^-/NO_2^-@CB_3 and NO_3^-/NO_2^-@CN_3 complexes were calculated in both gas and aqueous environments using Eq. (1), with basis set superposition error (BSSE) corrections applied.

Table 1. The adsorption energy (Eads) and Enthalpy (ΔH) of the interaction between NO_3/NO_2 ions and CB_3 and CN_3 nanoflakes at 298.15 to 328.15 K.

	$E_{ads\ (gas)}$ (kcal/mol)|	$E_{ads\ (w)}$ (kcal/mol)	μ (Debye)	α (a.u)	ΔH/ (kcal/mol) 298.15 K	ΔH/ (kcal/mol) 308.15 K	ΔH/ (kcal/mol) 318.15 K	ΔH/ (kcal/mol) 328.15 K
NO_2-CB_3-1	–38.78	–28.02	0.72	655.19	–39.40	–39.35	–39.30	–39.25
NO_2-CB_3-2	–73.46	–27.78	2.97	587.35	–73.21	–73.18	–73.15	–73.11
NO_2-CB_3-3	–38.78	–12.01	0.73	655.17	–39.40	–39.35	–39.30	–39.25
NO_2-CN_3-1	–43.12	–7.82	1.97	493.50	–42.88	–42.72	–42.56	–42.40
NO_2-CN_3-2	–43.02	–7.81	1.19	493.15	–42.87	–42.72	–42.56	–42.39
NO_2-CN_3-3	–16.61	–13.68	2.57	532.84	–16.60	–16.58	–16.42	–16.26
NO_3-CB_3-1	–45.54	–14.50	4.54	533.19	–45.63	–45.58	–45.53	–45.48
NO_3-CB_3-2	–45.54	–18.92	5.97	538.37	–45.64	–45.58	–45.53	–45.48
NO_3-CB_3-3	–51.04	–18.29	5.97	538.87	–51.02	–50.97	–50.92	–50.87
NO_3-CN_3-1	–7.31	–2.21	4.41	742.57	–7.29	–7.24	–7.19	–7.13
NO_3-CN_3-2	–11.70	–2.97	7.13	781.36	–7.31	–7.15	–6.99	–6.41
NO_3-CN_3-3	–13.88	–3.32	9.71	366.18	–13.83	–13.75	–16.50	–16.45

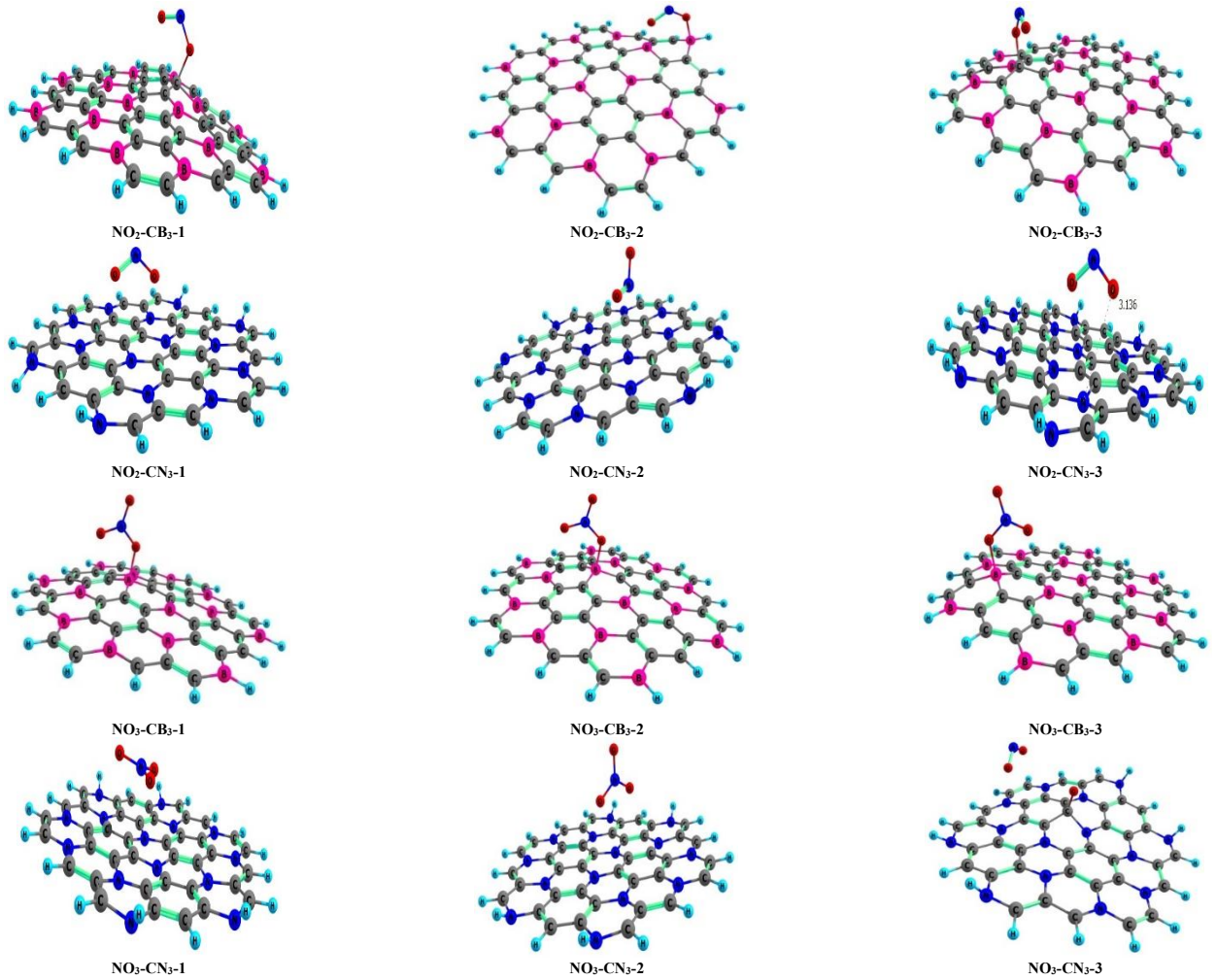


Figure 1. The optimized geometrical structures of the NO_3/NO_2@CB_3 and NO_3/NO_2@CN_3 complexes.

The corrected E_{ads} values are summarized in Table 1. In all cases, the adsorption energies are negative, confirming that the adsorption processes are exothermic. In the gas phase, the E_{ads} values of NO_2^-@CB_3 and NO_2^-@CN_3 complexes range from −38.78 to −73.46 kcal/mol and −16.61 to −43.12 kcal/mol, respectively. For the NO_3^-@CB_3 and NO_3^-@CN_3 complexes, the corresponding ranges are −45.54 to −51.04 kcal/mol and −7.31 to −13.88 kcal/mol, respectively. The strong and exothermic adsorption of NO_2^- and NO_3^- ions on CB_3 and CN_3 nanoflakes has important implications for water pollution control and environmental policy. The high adsorption energies observed for CB_3 indicate its strong capability to permanently immobilize nitrate and nitrite ions, offering a promising strategy for reducing nutrient loading in water resources and mitigating eutrophication. This is directly aligned with international water quality regulations that aim to limit nitrate and nitrite concentrations in drinking and surface waters. Meanwhile, the moderate interaction strength of CN_3 supports its potential use in recyclable adsorption systems and real-time monitoring technologies, contributing to sustainable and cost-effective water treatment solutions. These findings provide theoretical support for the development of advanced nanomaterials to meet increasingly stringent environmental standards for nitrogen-based pollutants.

In the water media, the E_{ads} values of NO_2^-@CB_3 and NO_2^-@CN_3 complexes range from −12.01 to −18.02 kcal/mol and −7.81 to −13.68 kcal/mol, respectively. For the NO_3^-@CB_3 and NO_3^-@CN_3 complexes, the

corresponding ranges are −14.50 to −18.92 kcal/mol and −2.21 to −3.32 kcal/mol, respectively. As expected, adsorption energies decrease in aqueous solution due to solvation effects and water shielding of both ions and nanoflakes. Nevertheless, among all studied systems, the CB_3–NO_2^-–2 complex exhibits the highest adsorption energy, indicating that CB_3 nanoflakes possess superior adsorption capability for both nitrate and nitrite ions and can be considered promising candidates for ion removal applications.

The dipole moment (μ) and mean polarizability (α) values further support the adsorption and sensing performance of these systems. For the NO_2^-@CB_3 and NO_2^-@CN_3 complexes, μ and α fall within the ranges of 0.72–2.97 Debye and 587.35–655.19 a.u., and 1.19–2.57 Debye and 493.15–531.18 a.u., respectively. In contrast, significantly higher values are observed for NO_3^-@CB_3 (μ = 4.54–5.97 Debye; α = 533.19–538.87 a.u.) and NO_3^-@CN_3 (μ = 4.41–9.71 Debye; α = 366.18–781.36 a.u.) complexes. The enhanced dipole moment and polarizability of the nitrate complexes suggest stronger charge redistribution and higher sensitivity in aqueous environments, which is highly desirable for ion adsorption and sensing applications.

3.2. Thermodynamic Parameters

Thermodynamic parameters calculated at 298.15, 308.15, 318.15, and 328.15 K (Table 1) indicate that both ΔH and ΔG values for all NO_3^-/NO_2^-@CB_3 and NO_3^-/NO_2^-@CN_3 complexes are negative in both gas and aqueous phases. These results confirm that the adsorption processes are exothermic and thermodynamically spontaneous over the entire temperature range. Notably, the ΔH values for the CB_3-based complexes are consistently more negative than those for CN_3-based systems, further demonstrating the superior adsorption performance of CB_3 nanoflakes. A slight decrease in ΔH is observed with increasing temperature from 298.15 to 328.15 K, indicating that temperature has a minimal influence on adsorption efficiency and that these nanoflakes remain effective ion adsorbents across a broad temperature range relevant to environmental applications. The minimal variation of ΔH with temperature suggests stable adsorption performance across environmentally relevant temperature ranges, highlighting the potential of CB_3 and CN_3 nanoflakes as robust and energy-efficient adsorbents for water purification applications.

Inspection of the results of Table S1 indicates that the value of the $\Delta\Delta G_{(sol)}$ parameter in all studied complexes is positive, while the value of $\Delta G_{(gas\text{-}sol)}$ in an aqueous medium is negative; therefore, the formation of NO_3^-/NO_2^-@CB_3 and NO_3^-/NO_2^-@CN_3 complexes in an aqueous medium is negative and spontaneous. On the other hand, the absolute values of Gibbs free energy in the water media are lower than in the gas media.

Finally, infrared (IR) spectra were analyzed to elucidate the nature of the interactions between the ions and nanoflakes (Fig. S2). The IR spectra of NO_3^-/NO_2^-@CN_3 complexes exhibit pronounced splitting and activation of nitrate vibrational modes, particularly the symmetric N–O stretching band in the 1000–1100 cm^{-1} region, indicating symmetry reduction and strong host–guest interactions within the CN_3 framework. Similarly, the IR spectra of NO_3^-/NO_2^-@CB_3 complexes show significant splitting and intensity enhancement of both symmetric and asymmetric N–O stretching modes. These features reflect strong Lewis acid–base interactions between nitrate oxygen atoms and boron centers, as well as substantial electronic perturbation of the CB_3 framework upon ion adsorption, confirming the formation of stable adsorption complexes.

3.3. Quantum Descriptors and HOMO and LUMO

3.3.1. HOMO-LUMO Orbitals

The electronic properties of the NO_3^-/NO_2^-@CB_3 and NO_3^-/NO_2^-@CN_3 complexes were investigated through analysis of the highest occupied molecular orbital (HOMO) and lowest unoccupied molecular orbital (LUMO) energies. Based on the calculated $E_{HOMO}$and E_{LUMO}values, key quantum chemical descriptors, including the energy gap (E_{gap}), chemical hardness (η), and electronic chemical potential (μ), were determined for all studied systems.

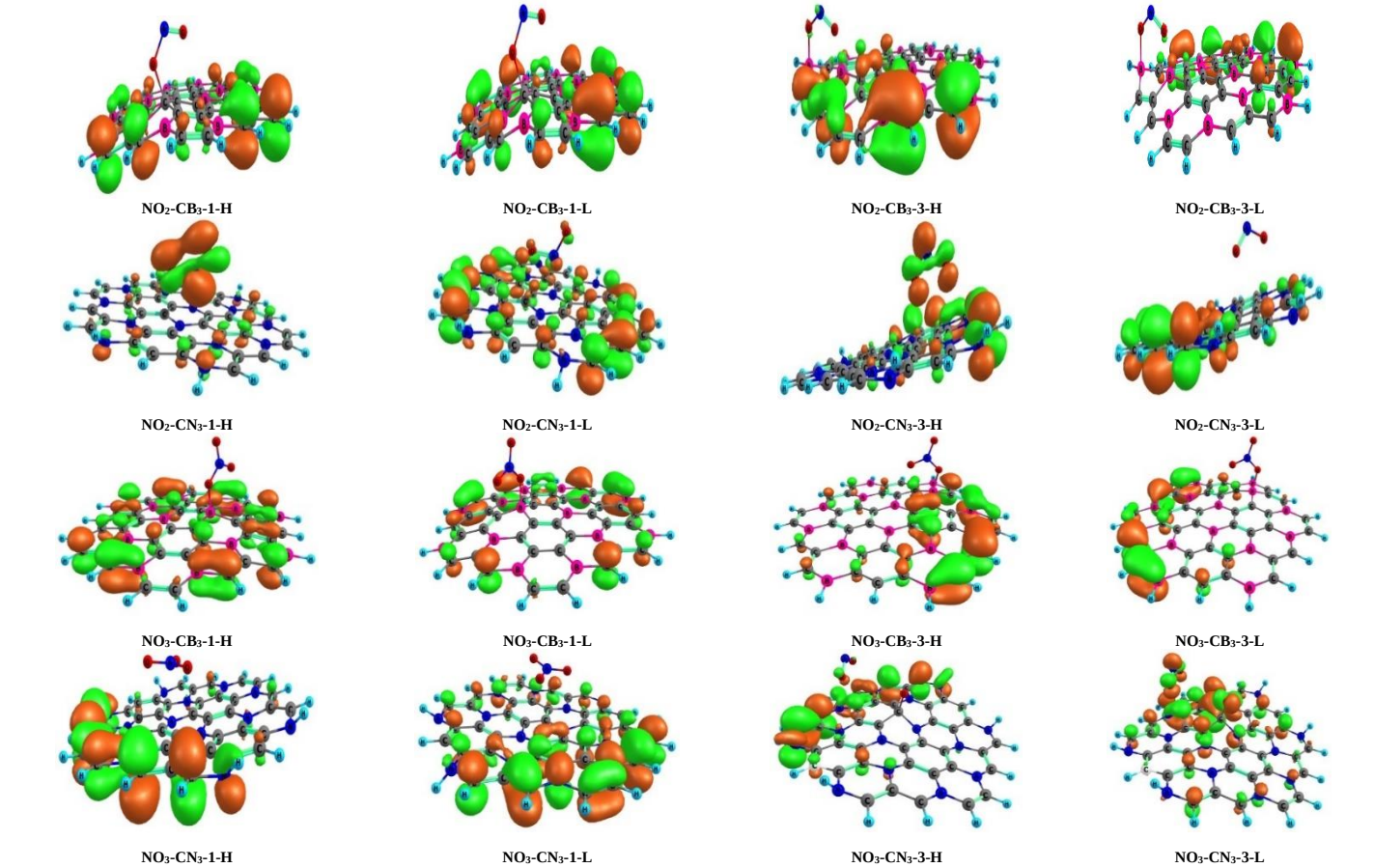


Figure 2. Plots of HOMO and LUMO orbital structures of the NO_3/NO_2@CB_3 and NO_3/NO_2@CN_3 complexes.

The corresponding results are summarized in Figure 2 and Table 2. As illustrated in Figure 2, the spatial distributions of the HOMO and LUMO for most NO_3^-/NO_2^-@CB_3 and NO_3^-/NO_2^-@CN_3 complexes are predominantly localized on the nanoflake surfaces. This orbital localization indicates that the CB_3 and CN_3 frameworks actively participate in charge transfer processes and are capable of interacting efficiently with both electrophilic and nucleophilic species. Such behavior is highly desirable for sensing applications, as it facilitates modulation of the electronic structure upon ion adsorption. Notably, in the NO_2^-@CN_3-1 complex, the HOMO density is mainly localized on the NO_2^- ion, suggesting that this region is particularly susceptible to electrophilic attack. This localized electronic behavior provides valuable insight into charge redistribution upon adsorption and can be exploited in the rational design of selective and efficient nanoflake-based sensors for nitrate and nitrite ion detection.

3.3.2. Density of States (DOS) Analysis

The electronic characteristics of the NO_3^-/NO_2^-@CB_3 and NO_3^-/NO_2^-@CN_3 complexes were further investigated through density of states (DOS) analysis. The total DOS spectra were calculated within the energy range of −15 to 10 eV, and the results are presented in Figure 3.

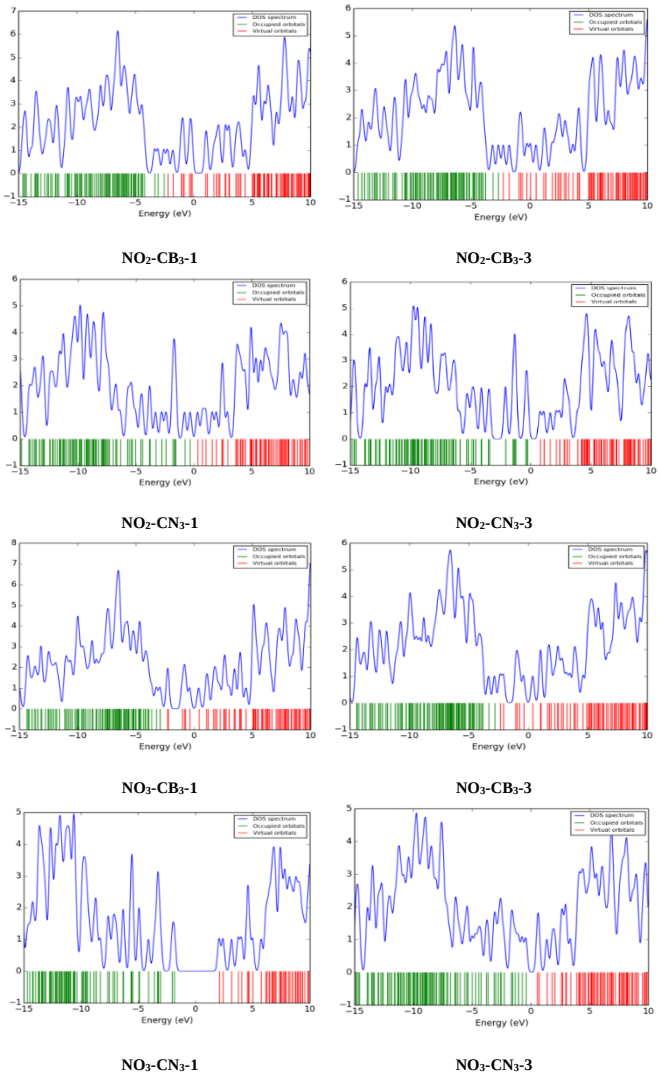


Figure 3. DOS plots of the NO_3/NO_2@CB_3 and NO_3/NO_2@CN_3 complexes.

The DOS profiles provide valuable insight into the distribution of electronic states near the Fermi level and their contribution to the electrical and optical behavior of the complexes. As shown in Figure 3, the number of prominent peaks in the vicinity of the HOMO and LUMO regions varies among the studied systems. For the NO_2^-@CB_3 complex, 14 and 15 peaks are observed in the HOMO and LUMO regions, respectively. In comparison, the NO_2^-@CN_3 complex exhibits a higher density of electronic states, with 18 HOMO-related and 23 LUMO-related peaks.

For nitrate adsorption, the NO_3^-@CB_3 complex shows 16 peaks in the HOMO region and 13 peaks in the LUMO region, while the NO_3^-@CN_3 complex displays 15 and 11 peaks in the corresponding regions. Notably, the intensity of the DOS peaks near the Fermi level follows the trend. NO_3^-/NO_2^-@CB_3 > NO_3^-/NO_2^-@CN_3. The higher peak intensities observed for the CB_3-based complexes indicate a greater contribution of electronic states near the frontier orbitals, which enhances charge-transfer capability and optical response. This increased electronic activity suggests that CB_3 nanoflakes are more effective platforms for signal modulation upon nitrate and nitrite adsorption, making them particularly suitable for sensing applications in environmental systems.

3.3.3. Quantum Chemical Descriptors

To quantitatively assess the electronic reactivity, conductivity, and stability of the NO_3^-/NO_2^-@CB_3 and NO_3^-/NO_2^-@CN_3 complexes, several quantum chemical descriptors were derived from the HOMO and LUMO energies. These descriptors include the energy gap ($E_{gap}=E_{LUMO}-E_{HOMO}$), global hardness ($\eta=(E_{LUMO}-E_{HOMO})/2$), and chemical potential ($\mu=(E_{HOMO}+E_{LUMO})/2$) as summarized in Table 2 [44–46].

Table 2. The quantum descriptors of the interaction of NO_3/NO_2 ions and CB_3, and CN_3 nanoflakes.

	E_{HOMO} (Ev)	E_{LUMO} (eV)	E_{gap} (eV)	η (eV)	μ (eV)
NO_2-CB_3-1	–2.56	–2.23	0.33	0.17	–2.39
NO_2-CB_3-2	–2.66	–2.24	0.42	0.21	–2.45
NO_2-CB_3-3	–2.56	–2.23	0.33	0.17	–2.39
NO_2-CN_3-1	–3.08	–2.33	0.75	0.37	–2.75
NO_2-CN_3-2	–0.91	–0.33	0.58	0.28	–0.62
NO_2-CN_3-3	–1.26	–0.78	0.46	0.23	–1.02
NO_3-CB_3-1	–2.91	–2.27	0.64	0.32	–2.59
NO_3-CB_3-2	–2.91	–2.27	0.64	0.32	–2.59
NO_3-CB_3-3	–2.84	–2.37	0.47	0.23	–2.60
NO_3-CN_3-1	–1.83	–1.08	0.75	0.37	–1.45
NO_3-CN_3-2	–1.42	–0.68	0.74	0.37	–1.03
NO_3-CN_3-3	–1.41	–0.57	0.84	0.42	–0.99

The HOMO–LUMO energy gap is a key indicator of electrical conductivity and sensing performance. Smaller E_{gap}values correspond to enhanced electron mobility and higher electrical conductivity. The calculated E_{gap}values for all studied complexes fall within the range of 0.33–0.84 eV, indicating semiconducting behavior and favorable sensitivity toward external perturbations induced by ion adsorption. Among the investigated systems, the NO_2^-@CB_3 complex exhibits the lowest E_{gap}, implying superior conductivity and a strong response to adsorption events. Global hardness (η) reflects the resistance of a system to charge transfer; lower values indicate higher chemical reactivity and easier electron excitation from the HOMO to the LUMO. Consistent with the energy gap analysis, the NO_2^-@CB_3 complex shows the smallest η value, confirming its enhanced reactivity and strong potential as a sensitive sensor material.

The chemical potential (μ) provides insight into the thermodynamic stability of the complexes. More negative μ values correspond to higher electronic stability. Comparison of the calculated results reveals the following trend in chemical potential: NO_3^-/NO_2^-@CB_3 > NO_3^-/NO_2^-@CN_3, indicating that the CB_3-based complexes possess greater overall stability than their CN_3 counterparts. Overall, the combined DOS and quantum descriptor analyses demonstrate that CB_3 nanoflakes exhibit enhanced electronic activity, higher conductivity, greater reactivity, and improved stability upon nitrate and nitrite adsorption. These features highlight CB_3 as a highly promising candidate for the design and development of efficient adsorbents and highly sensitive sensors for NO_3^- and NO_2^- ions in environmental monitoring and water purification applications.

3.4. UV-Visible Spectrum

Another method of identifying and tracking the drug to the nanoflakes in the body is to examine and analyze the UV-visible spectra. UV spectra refer to adsorption or reflection spectroscopy that appears in a part of the ultraviolet and visible regions of electromagnetic waves [47–48].

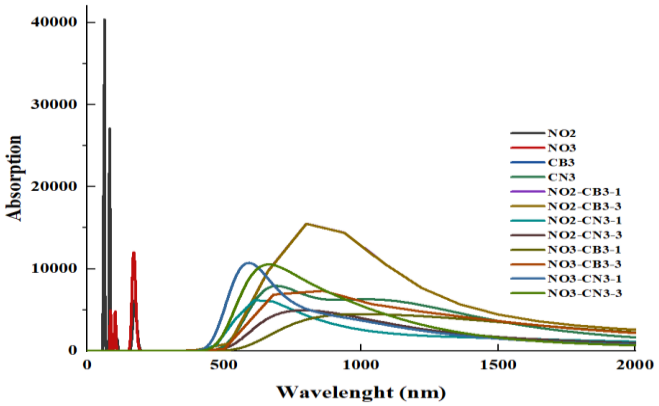


Figure 4. UV-visible spectra of NO_3/NO_2@CB_3 and NO_3/NO_2@CN_3 complexes.

The TD-DFT method is used to calculate UV spectra for 20 energy-level transitions, and the results are presented in Figures 4 and S4, and the transition states are listed in Table 3. The UV–visible absorption spectra of pristine NO_2, NO_3, CB_3, and CN_3 nanoflakes, as well as their corresponding adsorption complexes, are presented in the wavelength range of 0–2000 nm. The isolated NO_2 and NO_3 species exhibit intense absorption bands exclusively in the deep ultraviolet region (<300 nm), which originate from intrinsic $\mathbf{n} \rightarrow \boldsymbol{\pi}^*$ and $\boldsymbol{\pi} \rightarrow \boldsymbol{\pi}^*$ electronic transitions associated with the nitrogen–oxygen bonding framework. These sharp UV features indicate that the free ions have negligible optical activity in the visible and near-infrared (NIR) regions. In contrast, the pristine CB_3 and CN_3 nanoflakes display broad absorption bands extending from the visible to the NIR region (approximately 450–1200 nm). These bands are attributed to $\boldsymbol{\pi} \rightarrow \boldsymbol{\pi}^*$ transitions within the conjugated electronic structure of the nanoflakes, reflecting their semiconducting nature and relatively small

HOMO–LUMO energy gaps. Notably, CN_3 shows a slightly red-shifted absorption onset compared to CB_3, indicating stronger electronic delocalization and enhanced charge-transfer capability due to the presence of nitrogen atoms. Upon adsorption of NO_2 and NO_3 ions onto CB_3 and CN_3 surfaces, a pronounced enhancement and red shift of the absorption intensity is observed across the visible and NIR regions. The adsorption complexes exhibit new broad absorption features centered between ~550 and 1000 nm, which are absent in the spectra of the isolated components. These newly emerged bands are attributed to intermolecular charge-transfer (ICT) transitions between the adsorbed ions and the nanoflake surfaces, arising from strong electronic coupling and orbital hybridization. Furthermore, the CB_3- and CN_3-based complexes show adsorption-site-dependent spectral variations (models −1 and −3), where configurations with stronger adsorption energies exhibit higher absorption intensities and more pronounced bathochromic shifts. This behaviour confirms that the interaction strength directly modulates the electronic structure of the nanoflakes, leading to a reduction in the HOMO–LUMO gap, as supported by TD-DFT results. Overall, the significant red shift and enhanced absorption in the visible–NIR region upon NO_2 and NO_3 adsorption demonstrate that both CB_3 and CN_3 nanoflakes are highly sensitive optical platforms. The CN_3-based complexes, in particular, show stronger and broader absorption responses, suggesting superior performance for optical sensing and environmental monitoring of nitrate and nitrite pollutants. According to Table 3 for all complexes, the dominant absorption features arise from transitions originating from the ground state (S_0) to higher singlet excited states (S_n), with excitation wavelengths spanning the visible and near-infrared (NIR) regions (≈570–1070 nm). This broad spectral coverage is a clear indication that adsorption significantly modifies the electronic structure of the nanoflakes, enabling low-energy optical transitions. The main contributions to the excited states involve frontier molecular orbitals, primarily HOMO → LUMO**,** HOMO–1 → LUMO**,** and HOMO → LUMO+1 transitions, often with multiple orbital contributions.

Such mixed orbital character reflects strong orbital hybridization and electronic coupling between the adsorbed ions and the CB_3/CN_3 surfaces. The presence of multiple configurations with comparable weights confirms the delocalized nature of the excited states and supports the occurrence of intermolecular charge-transfer (ICT) excitations**.** In the NO_2–CB_3 complexes, absorption maxima appear mainly in the range of ≈700–890 nm, with moderate oscillator strengths (f ≈ 0.06–0.21), indicating optically allowed transitions. Among these, the NO_2–CB_3-1 configuration exhibits the highest oscillator strength, suggesting stronger light absorption due to more effective charge transfer between NO_2 and the CB_3 surface. For the NO_2–CN_3 complexes, the absorption bands are generally red-shifted compared to CB_3-based systems, extending up to ~960 nm. This behavior is associated with the higher electron affinity and enhanced π-conjugation of CN_3**,** which facilitates stronger electronic communication with the adsorbed NO_2 ion. The relatively high excitation wavelengths and non-negligible oscillator strengths confirm the suitability of CN_3 nanoflakes for visible–NIR optical sensing. In the case of NO_3 adsorption, both CB_3 and CN_3 systems show absorption features extending deeper into the NIR region, particularly for NO_3–CB_3-2 (λ ≈ 1069 nm). These low-energy transitions originate from HOMO-based orbitals localized on the nanoflake to LUMO/LUMO+n states with significant NO_3 contribution, clearly indicating ion-to-surface and surface-to-ion charge-transfer excitations. The NO_3**–**CN_3 complexes exhibit relatively higher excitation energies and oscillator strengths, reflecting stronger adsorption-induced perturbations of the electronic structure.

3.5. Atom in Molecules

To accurately understand the nature of the bond between the drug and the nanoflakes, the AIM method of Bader is used [40, 49–50] to calculate the topological parameters such as total electron density (ρ_{BCP}), total energy of (H_{BCP}), and Laplacian of electron density at critical points ($\nabla^2\rho_{BCP}$), by the Multiwfn package [51]

Table 3. UV transmissions related to the interaction of NO_2 and NO_3 ions with CB_3 and CN_3 nanoflakes

	EXCITED STATE	WAVE FUNCTION	EXCITED ENERGY	CONFIGURATIONS	*f*
NO_2-CB_3-1	S0→S9	892.44	1.3893	0.131 (H-5→L+1)- 0.108(H-4→L)+ 0.274 (H-3→L+1) - 0.206(H-2→L+1) +0.139(H-1→L+2)- 0.142(H-1→L+2)+ 0.261(H-2→L+3) - 0.455(H→L+2)	0.2152
NO_2-CB_3-2	S0→S15	718.66	1.7252	0.481(H-6→L)- 0.234(H-5→L+1)+ 0.150(H-4→L+1)- 0.353(H-3→L+1)	0.0639
NO_2-CB_3-3	S0→S16	698.88	1.7740	0.223(H-6→L)- 0.373(H-5→L)+ 0.274(H-3→L+1)- 0.1(H-2→L)+0.105(H-2→L+2)-0.26(H-1→L+4)+ 0.157(H→L+2)	0.1138
NO_2 -CN_3-1	S0→S19	595.94	2.0805	0.149(H-6→L)- 0.195(H-4→L+1)+ 0.138(H-3→L+1)- 0.243(H-1→L+2) +0.139(H-2→L+1)- 0.192(H→L+2)+ 0.123(H-1→L+3)- 0.125(H→L+2)	0.1037
NO_2 -CN_3-2	S0→S12	716.23	1.7311	0.451(H-6→L)- 0.108(H-5→L)+0.337(H-4→L)- 0.318(H-1→L+3)	0.0320
NO_2 -CN_3-3	S0→S6	959.38	1.2923	0.175(H-5→L)- 0.146(H-4→L)+0.526(H-1→L+1)- 0.366(H-1→L+2)	0.0545
NO_3-CB_3-1	S0→S14	821.56	1.5091	0.557(H-6→L)-0.339(H-6→L+1)+0.189 (H→L+2)	0.0106
NO_3-CB_3-2	S0→S8	1069.32	1.1595	0.186(H-5→L)- 0.185(H-4→L)+0.165(H-4→L+2)- 0.589(H-3→L)	0.0639
NO_3-CB_3-3	S0→S15	788.83	1.5718	0.109(H-7→L)- 0.286(H-6→L)+ 0.253(H-5→L+1)-0.108(H-4→L+1)+0.141(H-3→L+1) - 0.525(H→L+4)	0.0346
NO_3-CN_3-1	S0→S19	595.94	2.0805	0.149(H-6→L)- 0.195(H-4→L+1)+ 0.138(H-3→L+1)- 0.243(H-1→L+2) +0.139(H-2→L+1) - 0.192(H→L+2)+ 0.123(H-1→L+3) - 0.125(H→L+2)	0.1037
NO_3-CN_3-2	S0→S20	573.62	2.1615	0.162(H-5→L)- 0.104(H-5→L+1)+ 0.153(H-4→L)- 0.152(H-1→L+3)	0.2192
NO_3-CN_3-3	S0→S18	2.0617	601.38	0.143(H-7→L)- 0.111(H-3→L)+ 0.277(H-2→L+2)- 0.338(H-1→L+3)+0.135(H-→L+2)-0.142(H-1→L+2)+ 0.181(H-2→L+3)- 0.396(H-2→L+4)	0.0672

Table 4. Topological parameters (a.u) of AIM for the interaction of NO_3/NO_2 ions and CB_3, and CN_3 nanoflakes.

	ρ	H(r)	V(r)	$\nabla^2\rho$	ELF
NO_2-CB_3-1	0.1178	0.5103	–0.1089	–0.4355	0.9652
NO_2-CB_3-2	0.1178	0.5024	–0.1089	–0.4355	0.9236
NO_2-CB_3-3	0.6634	0.1087	–0.4208	–0.1683	0.9526
NO_2 -CN_3-1	0.3218	0.2955	–0.8090	–0.8722	0.6831
NO_2 -CN_3-2	0.3083	0.0971	–0.4005	–0.8248	0.9453
NO_2 -CN_3-3	0.3303	0.0513	–0.5056	–0.1612	0.9873
NO_3-CB_3-1	0.1179	0.0987	–0.1090	–0.4360	0.8598
NO_3-CB_3-2	0.1088	0.1765	–0.2409	–0.4487	0.1400
NO_3-CB_3-3	0.1728	0.3321	–0.4332	–0.9237	0.1769
NO_3-CN_3-1	0.0116	0.0089	–0.0078	–0.0401	0.0348
NO_3-CN_3-2	0.2857	0.2361	–0.6586	–0.7456	0.6943
NO_3-CN_3-3	0.2725	0.3914	–0.3085	–0.9211	0.9860

According results of Table 4, the nature of the interaction between NO_3^-/NO_2^- ions and CB_3 and CN_3 nanoflakes was investigated using the Atoms in Molecules (AIM) theory by analyzing the topological properties of the electron density at the bond critical points (BCPs). Key AIM parameters, including the electron density (ρ), Laplacian of electron density ($\nabla^2\rho$), total energy density (H(r)), potential energy density (V(r)), and electron localization function (ELF), provide valuable insight into the bonding mechanism and interaction strength.

The calculated electron density values (ρ) at the BCPs lie in the low to moderate range, confirming the formation of significant interactions between the ions and the nanoflake surfaces. Notably, higher ρ values are observed for several CN_3-based complexes compared to CB_3, indicating stronger binding interactions, which can be attributed to the enhanced electronegativity and electron-accepting capability of nitrogen atoms in the CN_3 lattice. A critical observation is that the Laplacian of the electron density is negative for all complexes ($\nabla^2\rho < 0$). A negative Laplacian indicates electron density concentration in the interaction region, which is characteristic of shared-shell interactions and implies a partial covalent or quasi-covalent character. This result demonstrates that the adsorption of NO_3^- and NO_2^- ions on CB_3 and CN_3 nanoflakes is not purely physisorptive, but involves a significant degree of chemical interaction and charge sharing. The potential energy density (V(r)) values are negative for all systems, confirming the stabilizing nature of the interactions. Moreover, the total energy density (H(r)) is negative or close to zero in several configurations, particularly for CN_3-based complexes, further supporting the presence of attractive interactions with partial covalent contributions. The dominance of V(r) over the kinetic energy density in these cases highlights the strength of the ion–surface interactions.

3.6. Electron Localization Function

The ELF (electron localization function) tool is used to understand the regions of molecular space where an electron pair is most likely to be found and the nature of the bond. In the ELF method, covalent and non-covalent interactions are identified with values larger and smaller than 0.5, and the nature of the bond is non-covalent [38, 52–53]. The ELF values provide additional insight into electron localization at the interaction regions.

High ELF values (ELF > 0.9), especially observed for NO_2–CB_3-1, NO_2–CN_3-3, and NO_3–CN_3-3, indicate significant electron localization, which is associated with stronger ion–surface interactions and enhanced charge transfer (see Table 4). In contrast, lower ELF values observed in weaker adsorption configurations reflect more diffuse and purely electrostatic interactions.

Overall, the AIM analysis demonstrates that the adsorption of NO_2 and NO_3 ions on both CB_3 and CN_3 nanoflakes is governed predominantly by electrostatic and charge-transfer-assisted noncovalent interactions. The CN_3 nanoflakes consistently exhibit higher electron density, stronger potential energy stabilization, and greater electron localization at the BCPs, confirming their superior interaction strength and sensing capability. These findings are in excellent agreement with the adsorption energy and UV–visible results, further validating CN_3 as a promising material for nitrate and nitrite detection and environmental remediation applications.

The color shades of ELF maps are delineated in Figure 5.

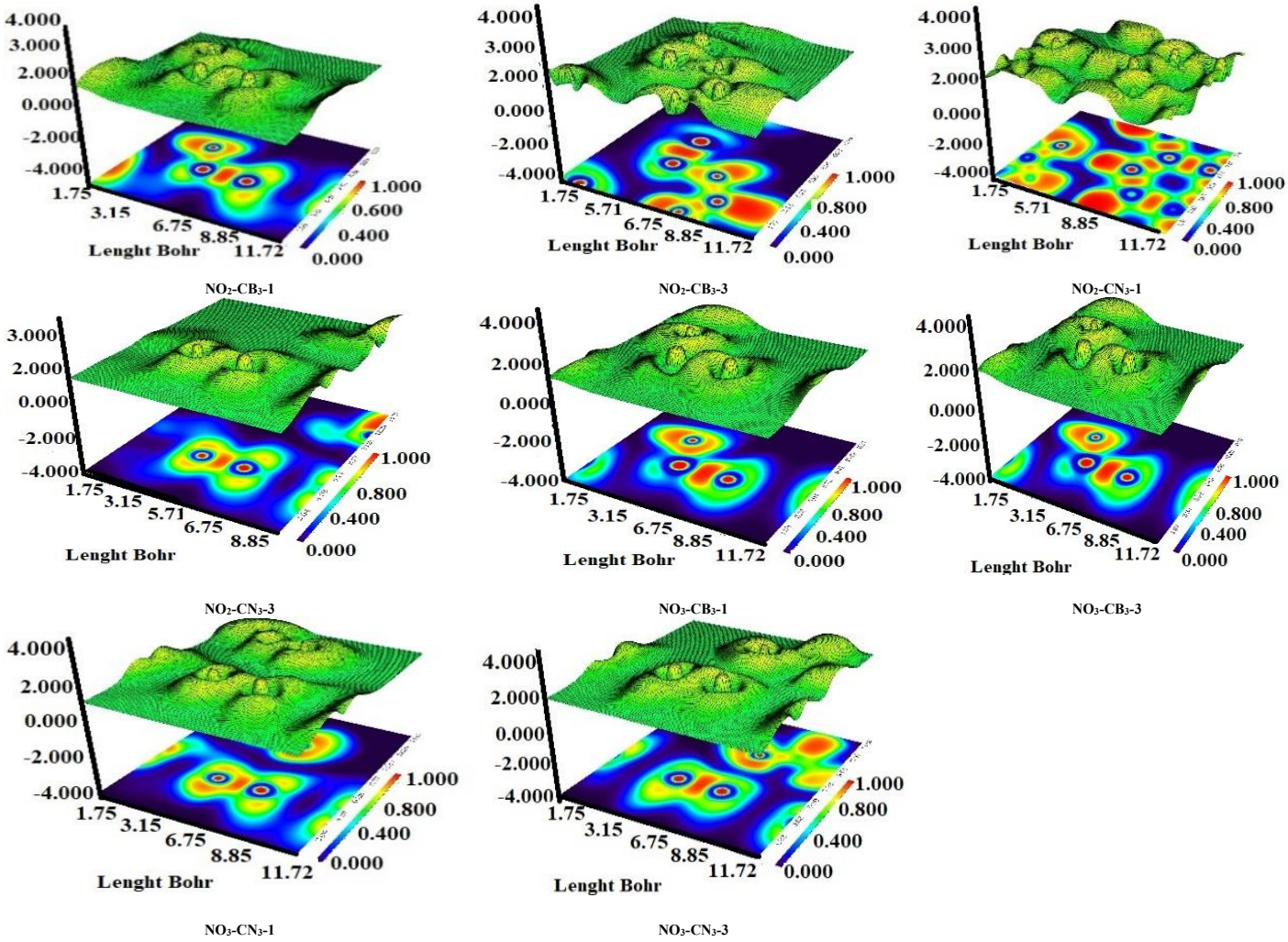


Figure 5. ELF plots of the NO_3/NO_2@CB_3 and NO_3/NO_2@CN_3 complexes.

As seen from Figure 5, the bluer color is localized between the NO_3/NO_2 and the CB_3/CN_3, which indicates the delocalized electron could be around it, and bespeak the region of electronic depletion between two compounds, so the interactions between NO_3/NO_2 with nanoflakes are noncovalent or van der Waals type.

3.7. Reduced Density Gradient Parameter

The reduced density gradient parameter (RDG) is one of the other quantum methods that can be used to study the nature of the bond between two compounds in detail, and its value is calculated from Eq.5 [55]:

$$RDG(r) = \frac{1}{2(3\pi^2)^{1/3}} \frac{|\nabla\rho(r)|}{\rho(r)^{4/3}} \quad (5)$$

The RDG scatter graphs and RDG isosurface for all NO_3/NO_2@CB_3> NO_3/NO_2@CN_3 complexes are displayed in Figure 6. In the RDG scatter graphs, the RDG values versus sign (λ_2) ρ(r) are delineated for the interaction NO_3/NO_2 with CB_3 and CN_3nanoflakes. According to Figure 6, the blue, green, and red colors are applied to determine the H-bonding, van der Waals, and strong repulsion interaction. The results of RDG scatter graphs (a) and RDG isosurface (b) revealed that most RDG of all studied complexes are localized in the λ=0 (with green color), so the interaction between NO_3/NO_2 with CB_3 and CN_3 nanoflakes is a van der Waals type. In the complex of NO_3 with NC_3, the most RDG is localized in the λ<0 (blue region) and λ=0 (green region), so the interaction between NO_3 with NC_3 nanoflakes is electrostatic and Van der Waals type. The RDG results confirm the AIM, ELF, and thermodynamic results.

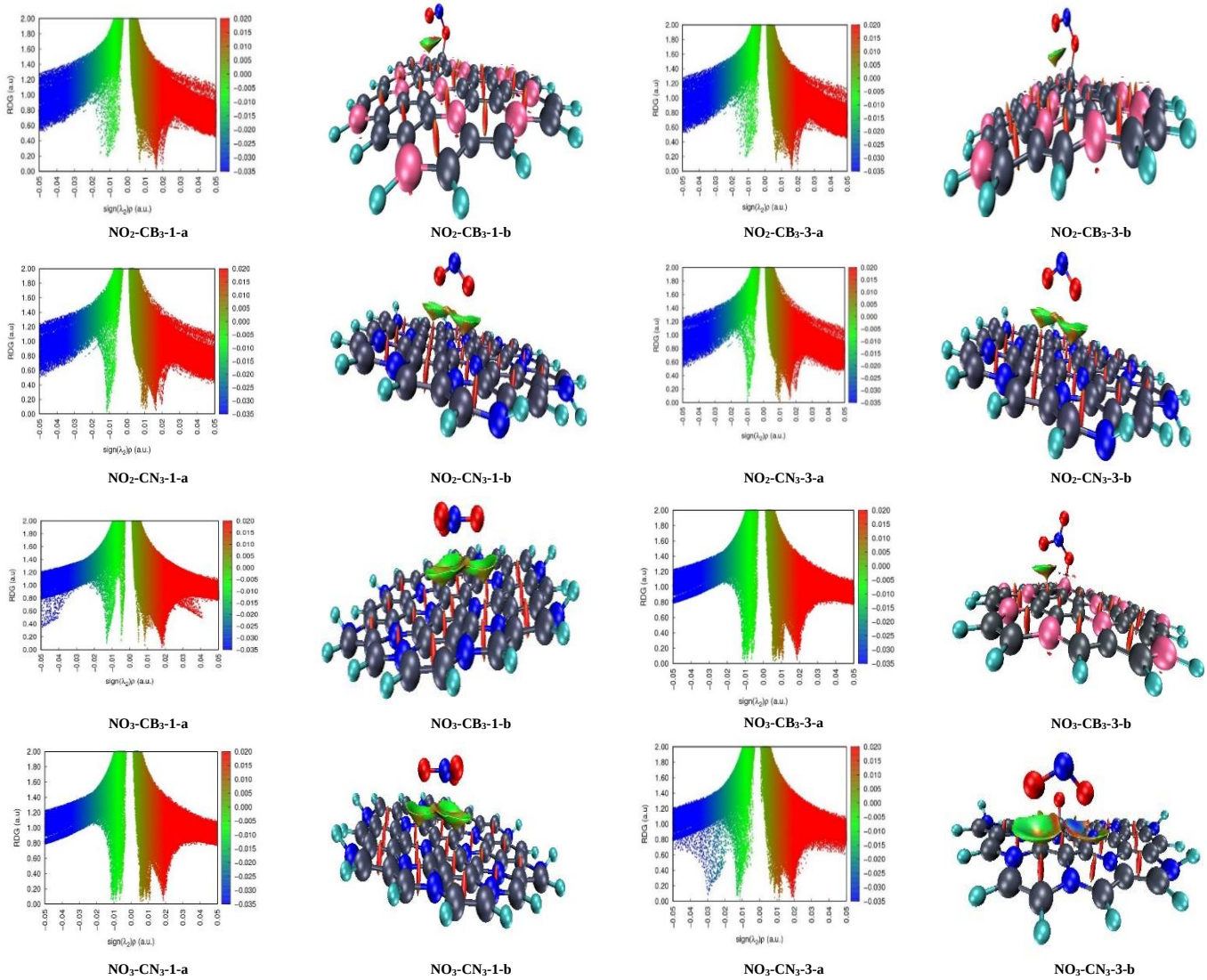


Figure 6. (a) RDG scatter graphs and (b) RDG isosurface of the NO_3/NO_2@CB_3 and NO_3/NO_2@CN_3 complexes.

4. Conclusions

In this work, the adsorption behavior and sensing potential of CB_3 and CN_3 nanoflakes toward nitrate (NO_3^-) and nitrite (NO_2^-) ions were systematically examined in both gaseous and aqueous environments using DFT and TD-DFT calculations at the ωB97XD/6-31+G(d, p) level of theory. The calculated gas-phase adsorption energies for NO_3^-@CB_3 (−45.54 to −51.04 kcal/mol) and NO_3^-@CN_3 (−7.31 to −13.88 kcal/mol) confirm strong and energetically favorable ion–surface interactions. Although solvation effects reduce adsorption strengths in aqueous media, the adsorption processes remain thermodynamically favorable. The NO_3^--adsorbed complexes exhibit significantly higher dipole moments and polarizabilities than their NO_2^- counterparts, indicating enhanced charge redistribution and superior sensing performance, particularly in water. Thermodynamic analyses demonstrate that all NO_3^-/NO_2^-@CB_3 and NO_3^-/NO_2^-@CN_3 complexes undergo exothermic and spontaneous adsorption in both phases over the temperature range of 298.15-328.15 K, with only minor temperature dependence. Electronic structure investigations reveal HOMO–LUMO energy gaps between 0.33 and 0.84 eV, reflecting semiconducting behavior and high sensitivity toward ion adsorption. Notably, the NO_2^-@CB_3 complex displays the smallest energy gap and chemical hardness, suggesting enhanced electrical conductivity and reactivity suitable for sensing applications. Furthermore, chemical potential analyses indicate greater electronic stability for CB_3-based complexes relative to CN_3 systems. Topological analyses using AIM, RDG, and ELF methods confirm that the adsorption mechanisms are predominantly governed by electrostatic interactions and van der Waals forces.

Overall, these findings highlight CB_3 nanoflakes as highly promising materials for the efficient detection and removal of nitrate and nitrite ions in water and wastewater treatment systems. Their strong, spontaneous, and thermodynamically stable adsorption characteristics support effective pollutant immobilization, thereby mitigating risks associated with eutrophication and water contamination. Consequently, CB_3-based nanomaterials emerge as environmentally relevant candidates for sustainable water monitoring and remediation technologies.

Acknowledgment

The author thanks the Computational Information Center of Malayer University for providing the necessary facilities to carry out the research.

Supplementary Data

Tables S1and Figures S1- S2 are given in supplementary data.

Credit authorship Contribution Statement

M. Abasi, and A Bagheri: Investigation and perform calculations, M. Rezaei-Sameti: Supervision, Project administration, and Manuscript writing and editing results.

Conflicts of Interest

The authors declare that they do not have any personal or financial conflicts of interest.

References

[1] U.S. Department of Health and Human Services, Agency for Toxic Substances and Disease Registry. *Toxicological Profile*, 2021.
[2] R. Picetti, M. Deeney. S. Pastorino. *Environmental Research*, 2022, **210**, 112988.
[3] *Environmental Science & Technology*, 2020, **54(5)**, 2345-2358.
[4] *Environmental Health*, 2019, **18(1)**, 1-12.
[5] T, Oku, M. Kuno, H. Kitahara, L. Narita. *International Journal of Inorganic Materials*, 2001, **3(7)**, 597-612.
[6] W. Choi, I. Lahiri, R. Seelaboyina, Y. S. Kang, *Critical Reviews in Solid State and Materials Sciences*, 2010, **35(1)**, 52-71.

[7] K. E. Whitener, P. E. Sheehan. *Diamond and Related Materials*, 2014, **46**, 25-34.
[8] V. Singh, D. Joung, L. Zhai, S. Das, S. I. Khndakero, S. Seal. *Progress in Materials Science*, 2011, **56(8)**, 1178-1271.
[9] K. S. Novoselov, A. K. Geim, S. V. Morozov, M. Jiang, M. Katsnelson, I. V. Grigorieva, S. V. Dubonos, S. V. Firsov, *Nature*, 2005, **438(7065)**, 197-200.
[10] M. Ghiasi, P. Zeinali, S. Gholami, M. Zahedi, *Journal of Molecular Modeling*, 2021, 27, 201.
[11] D. Golberg, Y. Bando, Y. Huang, T. Terao, M. Mitome, C. Tang, C. Zhi, *ACS Nano*, 2010, **4**, 2979-2993.
[12] H. Zeng, C. Zhi, Z. Zhang, X. Wei, X. Wang, W. Guo, Y. Bando, D. Golberg, *Nano Letters*, 2010, **10**, 5049-5055.
[13] C. R. Dean, A. F. Young, I. Meric, C. Lee, L. Wang, S. Sorgenfrei, K. Watanabe, T. Taniguchi, P. Kim, K. L. Shepard, J. Hone, *Nature Nanotechnology*, 2010, **5**, 722-726.
[14] A. Pakdel, C. Zhi, Y. Bando, T. Nakayama, D. Golberg, *ACS Nano*, 2011, **5,** 6507-6515.
[15] J. Yu, L. Qin, Y. Hao, S. Kuang, X. Bai, Y. M. Chong, W. Zhang, E. Wang, *ACS Nano*, 2010, **4**, 414-422.
[16] Q. Weng, X. Wang, X. Wang, Y. Bando, D. Golberg, *Chemical Society Reviews*, 2016, **45**, 3989-4012.
[17] W. T. Tee, N. Y. Li Loh, K. C. Lai, B. Y. Zhang Hiew, S. Gan, L. Y. Lee, *Separation and Purification Technology*, 2023, **320**, 124072.
[18] S. Sahu, S. Tiwari, *Elsevier*, 2023, 483-503.
[19] J. Beheshtian, A. A. Peyghan, Z. Bagheri, *Monatshefte Fur Chemie*, 2012, **143(12)**, 1623-1626.
[20] J. Beheshtian, M. Kamfiroozi, Z. Bagheri, A. A. Peyghan, *Chinese Journal of Chemical Physics*, 2012, **25(1)**, 60-64.
[21] V. P. Babar, S. Sharma, U. Schwingenschlögl, Advanced *Theory and Simulations*, 2018, **1(6)**, 1700008.
[22] X. Yuan, Y. Yong, Q. Hou, H. Cui, K. Tian, W. Ju, X. Li, X. Li, *SSRN*, 2023.
[23] F. Villanueva-Mejia, S. J. Guevara-Martínez, M. Arroyo-Albiter, J. Alvarado-Flores, A. Zamudio-Ojeda, *Nanomaterials*, 2023, **13(8)**, 1410.
[24] P. B. Ashishie, H. Louis, H. O. Edet, O. E. Offiong, A. Adeyinke, *Research Square*, 2023.
[25] C. Hu, B. Xiao, H. Wang, I. Muhammad, R. Liu, Y. Zhou, *Applications of Surface Science*, 2024, 159531.
[26] G. Mehraein, M. Rezaei-Sameti, E. Asgary, M. Aghamohammadi, *Journal of Molecular Structure*, 2022, **1248**, 131478.
[27] M. Rezaei-Sameti, A. Rajabi, *Chemical Papers*, 2023, **77**, 277-294.
[28] M. Rezaei-Sameti, Z. Iraji Borojeni, *Journal of Biomolecular Structure and Dynamics*, 2023, **41(4)**, 5882-5893.
[29] H. Darougari, M. Rezaei-Sameti, *Asian Journal of Nanoscience and Materials*, 2022, **5**, 196-210.
[30] M. Rezaei-Sameti, A. Rezaei, *Structural Chemistry*, 2023, **35(1)**, 1-14.
[31] M. Rezaei-Sameti, H. Torabi, *Journal of Computational Biophysics and Chemistry*, 2023, **22**, 1-18.
[32] M. L. Laury, A. K. Wilson, *Journal of Chemical Theory and Computation*, 2013, **9**, 3939-3946.
[33] *GaussView 3.0*, Gaussian, Inc., Carnegie Office Park - Building, 6 Pittsburg PA 15106 USA, 2000-2003.
[34] M. J. Frisch. et al. *Gaussian 09, Revision D.02*, Gaussian, Inc., Wallingford, CT, 2009.
[35] I. M. Felix, *Study of the Electronic Structure of Graphene and Hydrated Graphene*, 2013.
[36] P. K. Chattaraj, A, Poddar. *Journal of Physical Chemistry A*, 1999, **103**, 8691-8699.
[37] T. Koopmans, *Physica*, 1933, **1**, 104-113.
[38] A. Savin, *Journal of Molecular Structure*, 2005, **727**, 127-131.
[39] *IR spectrum of Busulfan drug*,
[40] R. F. W. Bader, *Atoms in Molecules: A Quantum Theory*, Oxford University Press, Oxford, U.K., 1990.
[41] E. R. Johnson, S. Keinan. P. Mori-Sanchez, J. Contreras-Garcia, A. Cohen, W. Yang, *Journal of the American Chemical Society*, 2010, **132**, 6498-6506.
[42] R. Daniel, D. Benjamin, G. Nageswara, H. Benjamin, M. Alexandre, H. Norberto, M. Mathieu, M. Leron, V. Eric, W. Victor, *ISRN Condensed Matter Physics*, 2021, 1-56.
[43] B. Mennucci, J. Tomasi, R. Cammi, J. R. Cheeseman, M. J. Frisch, F. J. Devlin, S. Gabriel, P, Stephens. *Journal of Physical Chemistry A*, 2002, **106**, 6102-6113.
[44] T. Koopmans, *Physica*, 1934, **1**, 104-113.
[45] R. G. Parr, R. G. Pearson, *Journal of the American Chemical Society*, 1983, **105**, 7512-7516.
[46] K. D. Sen, *Chemical Physics Letters*, 1991, 184, 318-320.
[47] T. C, Gregory. C. D, Reed. L. K, David. B. M, Angela. M. *Journal of Photochemistry and Photobiology A: Chemistry*, 2023, **437**, 114484.
[48] M. Cossi, V. Barone, *Journal of Chemical Physics*, 2001, **115**, 4708-4717.
[49] R. F. W. Bader, *Journal of Physical Chemistry A*, 1998, **102**, 7314-7323.
[50] R. F. W. Bader, *Canadian Journal of Chemistry*, 1998, 76, 973-988.
[51] S. Arulmozhi. J. Madhavan, *Materials Science and Engineering*, 2015, **73**, 012035.
[52] A. D. Becke, K. E. Edgecombe, *Journal of Chemical Physics*, 1990, **92(9)**, 5397-5403.
[53] A. Savin, O. Jepsen, J. Flad, O. K. Andersen, H. Preuss, H. von Schnering, *Angewandte Chemie International Edition in English*, 1992, **31(2)**, 187-188.
[54] V. Tsirelson, A. Stash, *Chemical Physics Letters*, 2002, **351**, 142-148.
[55] E. R. Johnson, S. Keinan, P. Mori-Sanchez, J. Contreras-Garcia, A. Cohen, W. Yang, *Journal of the American Chemical Society*, 2010, **132**, 6498-6506.